Improved Mean-Flow Solution for Slab Rocket Motors with Regressing Walls

Chong Zhou[*] and Joseph Majdalani[†]
Marquette University, Milwaukee, Wisconsin 53233

The Navier–Stokes equations are solved to obtain an approximate description of the mean flow in a slab rocket motor with two evenly regressing walls. The scope is limited to two-dimensional incompressible and chemically nonreactive viscous flow. The transformed governing equation is solved numerically, using finite differences, and asymptotically, using variation of parameters and small parameter perturbations in the blowing Reynolds number R. Results are correlated and compared via variations in R and the dimensionless wall regression rate. For hard blowing and moderate regression rates the effect of wall motion on the velocity is found to be small. Conversely, for fast-burning propellants, such as those being developed for high-acceleration vehicles, regression effects seem influential. Inclusion of viscous dissipation is also found to be important in assessing the total flow vorticity, especially when $R < 10^2$. The current geometric configuration is relevant to motor simulations using ducted channels with porous walls. For validation purposes comparisons with numerical solutions are carried out alongside end-process verifications. Because the resulting model incorporates viscosity and wall motion, it allows for an improved description of the unsteady acoustico-vortical solution whose assessment is strongly influenced by the mean flow.

Nomenclature

A	=	wall permeability coefficient, $v_w/\dot{a}$
A_b	=	burning, porous, or sublimating area, $2Wx^*$
A_c	=	flow cross section normal to the walls, $2aW$
A_p	=	dimensional oscillatory pressure amplitude
$\dot{a}$	=	dimensional wall regression speed
a_s	=	speed of sound
$a(t)$	=	half-height of simulated motor chamber
F	=	mean flow function, $\psi/x = f/R$
$I(x)$	=	integral function

$$\int_0^\theta \phi \csc \phi \, d\phi$$

k	=	dimensionless wave number, $\omega a/a_s$
L	=	internal chamber length
M	=	blowing Mach number, v_w/a_s
m	=	acoustic oscillation mode number
p	=	normalized pressure, $p^*/(\rho v_w^2)$
R	=	blowing Reynolds number, $v_w a/v$
r_ρ	=	solid-to-gas density ratio at the wall, ρ_S/ρ
Sr	=	Strouhal number, $\omega a/v_w$
t	=	dimensional time
(u, v)	=	axial and normal velocities, $(u^*/v_w, v^*/v_w)$
v_b	=	blowing velocity relative to the wall
v_w	=	absolute blowing velocity at the wall
W	=	motor width
x, y	=	dimensionless coordinates, $(x^*/a, y^*/a)$
α	=	wall regression ratio, $\dot{a}a/v$
ε	=	reciprocal of the blowing Reynolds number, R^{-1}
ε_p	=	pressure wave amplitude, $A_p/(\rho a_s^2)$

ζ	=	mean-flow vorticity, $a\zeta^*/v_w$
θ	=	characteristic variable, $(\pi/2)y$
ν	=	kinematic viscosity
ψ	=	mean-flow stream function, xF
ω	=	circular frequency, $(m-\frac{1}{2})\pi a_s/L$

Subscripts

a, n	=	axial and normal directions
b	=	blowing/burning relative to the wall
h	=	homogeneous part
m	=	spatial mean
S	=	solid phase
s	=	stagnation condition
tot	=	total, combines mean and unsteady parts
w	=	absolute wall condition
x, y	=	differentiation in x, y
0	=	initial condition
$*$	=	dimensional variable

I. Introduction

MATHEMATICAL models of internal gas dynamics in solid rocket motors have relied on subdividing the field variables into mean and time-dependent parts. Recent analyses by Flandro[1−3] and Majdalani et al.[4−13] have been helpful in providing time-dependent solutions that incorporate both viscous and rotational effects. In light of these findings, both viscous and rotational effects were shown to play important roles in prescribing the unsteady flow character. In particular, viscous dissipation was found to be a chief contributor to the damping of unsteady vorticity waves.[2−13] Its inclusion seemed clearly necessary for the correct assessment of time-dependent vorticity generation and evolution. These studies have also shown that unsteady vorticity could constitute a significant portion of the total flow vorticity and, as such, could play an important role in prescribing the global gas dynamics. This conclusion was first reached by Flandro[2,3] and was later reported by other investigators. It has been recently confirmed in the computational studies carried out by Apte and Yang[14−16] using nozzeless rocket motors. In fact, it will be further explored in this work.

The hydrodynamic stability of such flows has also received special treatment by Beddini,[17] Sabnis and Eagar,[18] Avalon et al.,[19] Casalis et al.,[20] and Griffond and Casalis.[21,22] The latter have used an original approach founded on linear instability theory. Accordingly,

the evolution of Taylor's solution to turbulence could be examined. In particular, their efforts have provided an alternative source of instability whose omission in classic analyses leads to discrepancies between theory and measurements. Hydrodynamic instabilities and the route to turbulence have also been numerically simulated by Liou and Lien[23] and Liou et al.[24,25] These recent studies have confirmed the presence of laminar conditions in elongated chambers not exceeding 20 in dimensionless length. They have also reported laminar segments in the head-end portions of longer chambers similar to those observed by other investigators (See Apte and Yang,[14] pp. 802, 803).

So far theoretical mean flow studies have only considered idealized motor chambers with stationary walls. In keeping pace with recent simulations of propellant burning, the need arises for a methodology that can lead to a regression-sensitive mean-flow solution. The current interest in developing fast-burning propellants for use in high-acceleration interceptor vehicles is one such example. The dedicated numerical simulations of propellant regression is another[26,27] (see also Fiedler, R. A., private communication, Center for Simulation of Advanced Rockets, Univ. of Illinois, Urbana–Champaign, 2001). The quest for a basic analytical solution is inspired, in part, by the desire for a theoretical element in a full-scale investigation. It is also motivated by modern developments of high-burn, high-energy propellants that lead to enhanced regression rates.[28] These trends to improve regression rates are also brought into perspective in the development of hybrid rocket engines. While the search for more suitable techniques to increase propellant burn rates continues, this article will present a basic methodology that permits the incorporation of wall regression in internal flow models.

The ability to incorporate viscous diffusion in mathematical idealizations of the injection-driven field constitutes another goal of this study. The reason is this. In the recent numerical simulations of nozzleless rocket motors, Apte and Yang[14–16] have determined that Taylor's inviscid mean-flow begins to degrade for $R < 500$ and becomes grossly in error for $R < 100$. According to Yuan[29] (p. 267), there are problems of real interest that exhibit crossflow Reynolds numbers of order 10. Under such circumstances, the use of Taylor's profile becomes inadequate. Another important motivation stems from the need to provide consistency in evaluating both mean and unsteady components of the flowfield developed by Flandro[1–3] and Majdalani et al.[4–6,9–13] In recent work by Majdalani,[8] a generalized higher-order approximation for the time-dependent field was presented; being of higher order, this formulation had the potential of increasing the precision of combustion stability predictions in use today. It also had the advantage of incorporating an arbitrary mean-flow function. Because the mean-flow expression must be fed into the time-dependent solution, it became logical to retain viscous and rotational effects in both mean and unsteady components of the flow. This could be attributed, in part, to the importance of viscous effects on the unsteady field (see Apte and Yang[14,15] or Majdalani[4] and Majdalani and Roh[10]). In that spirit the current paper will focus on presenting a rotational mean-flow solution that incorporates both viscosity and wall regression. The outcome should be a field that is consistently rotational and viscous in both its mean and time-dependent components.

Regarding the choice of geometry, ours corresponds to that of a slab rocket motor. Here the slab motor will be idealized as a long and nozzleless viscous channel with regressing porous walls. The same geometry has been used in the numerical studies reported by Apte and Yang[14] Despite the desire to account for common geometrical irregularities (such as inhibitors, igniters, submerged nozzles, interface gaps, conocyls, and slots),[18] the added mathematical complexities that accompany these items preclude closed-form solutions. One can only hope that analytical formulations of the type under investigation remain useful in unraveling basic physical aspects of the problem while helping to validate numerical simulations of more elaborate models (Fiedler, R. A., private communication, Center for Simulation of Advanced Rockets, Univ. of Illinois, Urbana–Champaign, 2001).

The article is organized as follows. The Navier–Stokes equations are first reduced to one fourth-order differential equation. The anal-

ysis then proceeds by applying similarity transformations in both space and time. These transformations evolve from the works of Berman,[30] Yuan and Finkelstein,[31] and Goto and Uchida.[32] On one hand, the spatial transformation takes advantage of flow similarity by presuming a linearly varying axial velocity. This spatial behavior is deduced from a mass balance in which the linear variation of the mean-flow axial velocity is proven. On the other hand, the temporal transformation assumes a constant dimensionless expansion ratio that corresponds to porous walls whose expansion speed diminishes with the distance from the core. Such a choice is consistent with a slab rocket motor undergoing a regressive burn. A regressive burn is expected of homogeneous propellants as a result of the expansion of the internal chamber volume with the passage of time. Under these auspices the two-dimensional Navier–Stokes equations collapse into a nonlinear differential equation that can be solved both numerically and asymptotically.

The equation obtained will be shown to reduce to the known Berman form when the porous walls are made motionless.[30] Additionally, the asymptotic solution will be shown to reduce to Taylor's[33] or Yuan's[29] for large injection in porous channels with stationary walls. From the analytical solution closed-form expressions will then be obtained for the velocity, vorticity, pressure, and shear at the wall. These will be used to characterize the flow. Subsequent comparisons with the numerical solution will gauge the accuracy of the analytical formulations over a range of moderate-to-high Reynolds numbers. In the process our original application of the method of variation of parameters will be validated.

II.   Mathematical Model

The slab rocket motor is modeled as a channel with porous walls. One side of the cross section, representing the distance $(2a)$ between the porous walls is taken to be smaller than the other two (W and L). This enables us to treat the problem as a case of two-dimensional flow. Both sidewalls are assumed to have equal permeability and to expand uniformly at a time-dependent rate $\dot{a}$. Inasmuch as the forthcoming similarity solution obviates the need to specify a finite body length L, one has the liberty of assuming a semi-infinite length.[34] To accommodate expanding boundaries, the head end is closed by a compliant membrane that is allowed to stretch with channel expansion.

As shown in Fig. 1, a coordinate system can be chosen with the origin at the center of the channel. Using the asterisk to denote dimensional variables, x^* and y^* are used to define the axial and normal coordinates. The corresponding axial and normal velocity components are defined by u^* and v^*. For uniform wall injection symmetry at $y^* = 0$ reduces the domain of investigation to $0 \leq y^* \leq a$.
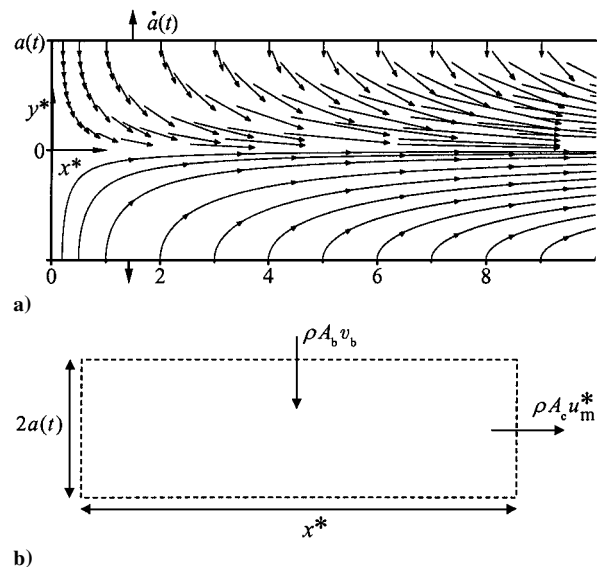

Fig. 1   Schematic of the chamber showing: a) the bulk gas motion using a standard coordinate system and b) the control volume used in applying mass conservation.

A. Governing Equations

For two-dimensional laminar and incompressible flow with no body forces, the differential expressions for mass and momentum conservation can be written as

$$\frac{\partial u}{\partial x} + \frac{\partial v}{\partial y} = 0 \tag{1}$$

$$\frac{a}{v_w}\frac{\partial u}{\partial t} + u\frac{\partial u}{\partial x} + v\frac{\partial u}{\partial y} = -\frac{\partial p}{\partial x} + \frac{1}{R}\left(\frac{\partial^2 u}{\partial x^2} + \frac{\partial^2 u}{\partial y^2}\right) \tag{2}$$

$$\frac{a}{v_w}\frac{\partial v}{\partial t} + u\frac{\partial v}{\partial x} + v\frac{\partial v}{\partial y} = -\frac{\partial p}{\partial x} + \frac{1}{R}\left(\frac{\partial^2 v}{\partial x^2} + \frac{\partial^2 v}{\partial y^2}\right) \tag{3}$$

given

$$x \equiv x^*/a, \qquad y \equiv y^*/a, \qquad u \equiv u^*/v_w$$

$$v \equiv v^*/v_w, \qquad p \equiv p^*/\rho v_w^2, \qquad R \equiv av_w/\nu \tag{4}$$

where ρ is the dimensional density. The idealized boundary conditions demand, as usual, no slippage at the wall in the parallel velocity component. They also require a uniform influx in the normal direction. These conditions translate into

$$u(x, 1) = 0 \text{ (no slip along the wall)}$$

$$v(x, 1) = -1 \text{ (uniform influx)} \tag{5}$$

For even blowing at the opposing walls, symmetry about the midsection plane requires that

$$\frac{\partial u}{\partial y}(x, 0) = 0, \qquad v(x, 0) = 0 \tag{6}$$

Furthermore, for no flow through the head end wall one must have

$$u(0, y) = 0 \text{ (impervious head end wall)} \tag{7}$$

Before applying these boundary conditions to the Navier–Stokes equations, some mass conservation considerations can be instructive in unravelling useful properties of the flow variables.

B. Injection and Regression Speeds

At the wall it is assumed that the absolute inflow velocity v_w is independent of position. One must also realize that the blowing or burning speed v_b with respect to the wall must be uniform along the length of the chamber because $v_w \equiv v_b - \dot{a}, \dot{a} \equiv da/dt$. The absolute speed of the injectant v_w is slightly reduced as a result of wall regression. This wall regression rate $\dot{a}$ coincides with the burning rate in a solid-propellant rocket motor.

Although v_w and $\dot{a}$ might be independent in cold-flow studies, they are related via the solid-to-gas density ratio owing to mass conservation at the propellant surface. If $A_b = 2Wx^*$ represents the burning surface in a solid propellant (or, alternatively, the sublimating surface in a cold-flow simulation[35−38]), then conservation of mass at the burning or sublimating interface requires that $\rho A_b v_b = \rho_S A_b \dot{a}$. The gas velocity with respect to the wall becomes

$$v_b = (\rho_S/\rho)\dot{a} \equiv r_\rho \dot{a} \tag{8}$$

where ρ_S is the density of the solid phase (before solid-propellant pyrolysis or hard-wall sublimation). From Eq. (8) the absolute velocity can be seen to be $v_w = (r_\rho - 1)\dot{a} = A\dot{a}$, where $A = r_\rho - 1$ is the injection coefficient.[32] Because $A \equiv v_w/\dot{a}$, it is a measure of wall permeability. In rocket motors $\rho_S \sim 2000 \text{ kg m}^{-3}$ (Ref. 39), $\rho \sim 20 \text{ kg m}^{-3}$ (Ref. 40), and $A \sim r_\rho \sim 100$. For a cold-flow experiment in which the walls are allowed to expand in the absence of forced injection (for example, for hard walls), v_b will be zero, and one obtains $v_w = -\dot{a}$ or $A = -1$.

III. Reduction of the Flow Equations

A. Development of the Similarity Form

By applying mass conservation to a deformable control volume extending from $x = 0$ to an arbitrary downstream position, the average flow velocity $u_m = u_m^*/v_w$ can be determined. Based on

$$\frac{\partial}{\partial t}\int_V \rho \, dV - \rho A_b v_b + \rho u_m^* A_c = 0 \tag{9}$$

where $V = A_c x^*$, and $A_c = 2aW$, one can integrate the temporal term from 0 to x^*. After some rearrangement one obtains

$$u_m = \frac{A_b}{A_c}\frac{v_b}{v_w} - \frac{ax}{A_c v_w}\frac{\partial A_c}{\partial t} = \frac{x(v_b - \dot{a})}{v_w} = x \tag{10}$$

Because the defining integral $u_m A_c = \int u \, dA$ is carried out with respect to y only, it follows that the property $u_m \propto x$ can be realized if, and only if, the axial velocity u is a linear function of x. This result provides the principal motivation for attempting a similarity transformation.

B. Vorticity-Stream Function Equations

To apply the correct similarity transformation, it is expedient to introduce the Stokes stream function and replace both velocity components by one single variable. This can be accomplished via $(u, v) = (\psi_y, -\psi_x)$, where $\psi \equiv \psi^*/(av_w)$. Pressure can also be eliminated from the momentum equation. This can be accomplished by taking the curl of the momentum equation. One obtains the vorticity transport equation, namely,

$$\frac{a}{v_w}\frac{\partial \zeta}{\partial t} + \frac{\dot{a}}{v_w}\frac{\partial u}{\partial y} + u\frac{\partial \zeta}{\partial x} + v\frac{\partial \zeta}{\partial y} = \frac{1}{R}\left(\frac{\partial^2 \zeta}{\partial x^2} + \frac{\partial^2 \zeta}{\partial y^2}\right) \tag{11}$$

where the vorticity is given by

$$\zeta \equiv \frac{a\zeta^*}{v_w} = \frac{\partial v}{\partial x} - \frac{\partial u}{\partial y} \tag{12}$$

C. Similar Solution in Space

As explained in Sec. IIIA, a similar solution with respect to x can be anticipated as a result of mass conservation. Following Berman's classic approach,[30] this similarity solution can be initiated by setting[41] $\psi = xf(y, t)/R$, where $f(y, t)$ is independent of the axial coordinate. Forthwith, the axial and normal velocities become $(u, v) = (xf_y/R, -f/R)$, where $f_y = \partial f/\partial y$. As v is independent of x, the vorticity equation becomes $\zeta = -u_y$, whereby Eq. (3) reduces to $p_{yx} = 0$. Upon substitution into the vorticity transport equation, one collects

$$\frac{x}{R^2}f_{yyyy} + \frac{\dot{a}}{v_w}\frac{x}{R}f_{yy} + \frac{a}{v_w}\frac{\partial}{\partial t}\left(-\frac{x}{R}f_{yy}\right)$$

$$+ \frac{x}{R}f_y\frac{\partial}{\partial x}\left(-\frac{x}{R}f_{yy}\right) - \frac{x}{R}f\frac{\partial}{\partial y}\left(-\frac{x}{R}f_{yy}\right) = 0 \tag{13}$$

Subsequent application of the chain rule leads to

$$\frac{x}{R^2}f_{yyyy} + 3\frac{x\alpha}{R^2}f_{yy} + \frac{xy\alpha}{R^2}f_{yyy} - \frac{x}{R^2}f_y f_{yy}$$

$$+ \frac{x}{R^2}ff_{yyy} - \frac{\nu x}{v_w^2}f_{yyt} = 0 \tag{14}$$

which simplifies into

$$f_{yyyy} + 3\alpha f_{yy} + \alpha y f_{yyy} - f_y f_{yy} + f f_{yyy} - a^2\nu^{-1}f_{yyt} = 0 \tag{15}$$

where $\alpha \equiv \dot{a}a/\nu$ is the wall regression ratio. Physically, this parameter represents the Reynolds number based on the normal speed of the walls. In cold-flow experiments R and α can be independent. In solid rocket motors, however, these two parameters are related by the injection coefficient A. Because $v_w = (r_\rho - 1)\dot{a} = A\dot{a}$, multiplication by a/ν yields $R = A\alpha$.

D. Similar Solution in Space and Time

A similar solution with respect to both space and time can now be developed following Uchida and Aoki.[34] Using the transformation $f(y, t) \to f[y, \alpha(t)]$ and assuming constant α, the last term in Eq. (15) can be suppressed. To realize this condition, the value of the regression ratio must be specified by its initial value, namely,

$$\alpha = \dot{a}a/\nu = \dot{a}_0 a_0/\nu \tag{16}$$

where a_0 and $\dot{a}_0$ denote the initial chamber half-height and wall regression rate. The temporal similarity transformation can be realized by integrating Eq. (16) with respect to time. Consequently, a similar solution for the temporal channel height is identified, namely, $a(t) = a_0\sqrt{(1 + 2\nu\alpha t a_0^{-2})}$.

E. Normalized Equations

At this juncture it is convenient to let $F \equiv f/R$. The normalized equations become

$$(\psi, \zeta) = (xF, -xF_{yy}), \qquad (u, v) = (xF_y, -F)$$

$$u/u_m = u/x = F_y \tag{17}$$

$$\varepsilon F_{yyyy} + \alpha\varepsilon(yF_{yyy} + 3F_{yy}) + FF_{yyy} - F_y F_{yy} = 0, \qquad \varepsilon \equiv R^{-1} \tag{18}$$

The exact solution of the problem becomes contingent on finding a solution F that satisfies

$$F_{yy}(0) = 0, \qquad F(0) = 0, \qquad F_y(1) = 0, \qquad F(1) = 1 \tag{19}$$

Note that Berman's equation[30] is a special case of Eq. (18) that can be restored by suppressing α.

IV. Analytical Solution

For moderate-to-large values of the Reynolds number, Eq. (18) can be solved asymptotically following a unique application of the variation of parameters technique. By virtue of the small parameter ε multiplying the highest derivative, a regular perturbation expansion of the form $F = F_0 + \varepsilon F_1 + \mathcal{O}(\varepsilon^2)$ can be attempted. Substitution into Eq. (18) gives, at $\mathcal{O}(1)$,

$$F_0 F_{0yyy} - F_{0y} F_{0yy} = 0 \tag{20}$$

with $F_0'(1) = 0$, $F_0(1) = 1$, $F_0(0) = 0$. The nonlinear form of Eq. (20) is not susceptible to known integration technique. It must be obtained by guessing that $F_0 = \sin\theta$, where $\theta \equiv \frac{1}{2}\pi y$.

A. First-Order Equation

Terms of $\mathcal{O}(\varepsilon)$ can be gathered and separated. The emerging first-order equation becomes

$$F_0 F_{1yyy} - F_{0y} F_{1yy} - F_{0yy} F_{1y} + F_{0yyy} F_1$$

$$= -F_{0yyyy} - 3\alpha F_{0yy} - \alpha y F_{0yyy} \tag{21}$$

This needs to be solved while satisfying

$$F_{1y}(1) = 0, \qquad F_1(1) = 0, \qquad F_1(0) = 0 \tag{22}$$

Switching to θ as the independent variable and using $F_0 = \sin\theta$, Eq. (21) becomes

$$\sin\theta F_1''' - \cos\theta F_1'' + \sin\theta F_1' - \cos\theta F_1$$

$$= \left(6\alpha/\pi - \tfrac{1}{2}\pi\right)\sin\theta + (2\alpha/\pi)\theta\cos\theta \tag{23}$$

with

$$F_1'\left(\tfrac{1}{2}\pi\right) = 0, \qquad F_1\left(\tfrac{1}{2}\pi\right) = 0, \qquad F_1(0) = 0 \tag{24}$$

B. Solving by Variation of Parameters

The solution of Eq. (23) must be carefully constructed. First, one can attempt to solve the homogeneous equation

$$\sin\theta F_1''' - \cos\theta F_1'' + \sin\theta F_1' - \cos\theta F_1 = 0 \tag{25}$$

To that end, one simple solution exhibited by Eq. (25) can be guessed to be $F_{1h} = \cos\theta$. Having determined one independent solution, the method of variation of parameters can be applied. This requires setting $F_{1h} = C(\theta)\cos\theta$, where $C(\theta)$ is unknown. Differentiation gives

$$F_{1h}' = C'\cos\theta - C\sin\theta$$

$$F_{1h}'' = C''\cos\theta - 2C'\sin\theta - C\cos\theta$$

$$F_{1h}''' = C'''\cos\theta - 3C''\sin\theta - 3C'\cos\theta + C\sin\theta \tag{26}$$

Subsequent substitution into Eq. (25) yields $C'''\sin\theta\cos\theta - 2C''\sin^2\theta - C'' = 0$. Thus C can be determined to be $C(\theta) = P_0\tan\theta + P_1\theta + P_2$, where P_0, P_1, and P_2 are integration parameters. This completes the expression for the general homogeneous solution

$$F_{1h} = P_0\sin\theta + P_1\theta\cos\theta + P_2\cos\theta \tag{27}$$

To make headway, a second-level parametric variation of P_0, P_1, and P_2 must be allowed. At the outset Eq. (27) becomes

$$F_1(\theta) = P_0(\theta)\sin\theta + P_1(\theta)\theta\cos\theta + P_2(\theta)\cos\theta$$

$$\equiv P_0(\theta)F_{1A}(\theta) + P_1(\theta)F_{1B}(\theta) + P_2(\theta)F_{1C}(\theta) \tag{28}$$

This term needs to be differentiated thrice before substitution into Eq. (23). The first differentiation yields

$$F_1' = P_0'F_{1A} + P_0 F_{1A}' + P_1'F_{1B} + P_1 F_{1B}' + P_2'F_{1C} + P_2 F_{1C}' \tag{29}$$

A procedural constraint binding the derivatives is $P_0'F_{1A} + P_1'F_{1B} + P_2'F_{1C} = 0$. Hence, by virtue of $P_0'\sin\theta + P_1'\theta\cos\theta + P_2'\cos\theta = 0$, Eq. (29) becomes

$$F_1' = P_0 F_{1A}' + P_1 F_{1B}' + P_2 F_{1C}'$$

$$= P_0\cos\theta + P_1(\cos\theta - \theta\sin\theta) - P_2\sin\theta \tag{30}$$

Differentiating a second time renders

$$F_1'' = P_0'F_{1A}' + P_0 F_{1A}'' + P_1'F_{1B}' + P_1 F_{1B}'' + P_2'F_{1C}' + P_2 F_{1C}'' \tag{31}$$

Letting $P_0'F_{1A}' + P_1'F_{1B}' + P_2'F_{1C}' = 0$ gives another constraint: $P_0'\cos\theta + P_1'(\cos\theta - \theta\sin\theta) - P_2'\sin\theta = 0$. Equation (31) becomes

$$F_1'' = P_0 F_{1A}'' + P_1 F_{1B}'' + P_2 F_{1C}''$$

$$= -P_0\sin\theta - P_1(2\sin\theta + \theta\cos\theta) - P_2\cos\theta \tag{32}$$

Finally, differentiating a third time brings about

$$F_1''' = -P_0'\sin\theta - P_0\cos\theta - P_1'(2\sin\theta + \theta\cos\theta)$$

$$- P_1(3\cos\theta - \theta\sin\theta) - P_2'\cos\theta + P_2\sin\theta \tag{33}$$

We now substitute F_1 and its derivatives, given by Eqs. (28), (30), (32), and (33), back into the complete first-order equation, given by Eq. (23). The result is

$$-P_0'\sin^2\theta - 2P_1'\sin^2\theta - P_1'\theta\sin\theta\cos\theta - P_2'\sin\theta\cos\theta$$

$$= (6\alpha/\pi - \pi/2)\sin\theta + (2\alpha/\pi)\theta\cos\theta \tag{34}$$

Equation (34) contains three unspecified functions P_0', P_1', and P_2'. To obtain closure, the two procedural constraints introduced earlier must be employed alongside Eq. (34). One finds

$$P_0'(\theta) = \frac{\alpha\theta \cos^3\theta}{\pi \sin^2\theta} - \left(\frac{\pi}{4} - \frac{3\alpha}{\pi}\right)\frac{\cos^2\theta}{\sin\theta}$$

$$P_1'(\theta) = \left(\frac{\pi}{4} - \frac{3\alpha}{\pi}\right)\frac{1}{\sin\theta} - \frac{\alpha\theta \cos\theta}{\pi \sin^2\theta}$$

$$P_2'(\theta) = \left(\frac{\pi}{4} - \frac{3\alpha}{\pi}\right)\left(\cos\theta - \frac{\theta}{\sin\theta}\right) - \frac{\alpha\theta \cos^2\theta}{\pi \sin\theta} + \frac{\alpha\theta^2 \cos\theta}{\pi \sin^2\theta}$$

$$(35)$$

Integrating for the variable parameters, one gathers, after some algebra,

$$P_0(\theta) = -\frac{\alpha}{\pi}(\theta/\sin\theta + \theta \sin\theta) + (2\alpha/\pi - \pi/4)\cos\theta$$
$$+ (4\alpha/\pi - \pi/4)\,\ell n \tan(\theta/2) + K_0$$

$$P_1(\theta) = (\pi/4 - 4\alpha/\pi)\,\ell n \tan(\theta/2) + (\alpha/\pi)(\theta/\sin\theta) + K_1$$

$$P_2(\theta) = (\pi/4 - 2\alpha/\pi)\sin\theta - \frac{\alpha}{\pi}(\theta \cos\theta + \theta^2/\sin\theta)$$
$$+ (4\alpha/\pi - \pi/4)I(\theta) + K_2 \tag{36}$$

where K_0, K_1, and K_2 are constants and

$$I(\theta) \equiv \int_0^\theta \phi \csc\phi \, d\phi = \theta$$
$$+ 2\pi \sum_{k=1}^\infty \left(\sum_{n=1}^\infty \frac{1}{n^{2k}}\right)\frac{(1 - 2^{1-2k})}{(2k+1)}\left(\frac{\theta}{\pi}\right)^{2k+1} \tag{37}$$

Inserting Eq. (36) into Eq. (28) yields, at length,

$$F_1 = -(2\alpha/\pi)\theta + (4\alpha/\pi - \pi/4)\big[(\sin\theta - \theta \cos\theta)\,\ell n \tan\tfrac{1}{2}\theta$$
$$+ \cos\theta I(\theta)\big] + K_0 \sin\theta + K_1\theta \cos\theta + K_2 \cos\theta \tag{38}$$

Applying the three boundary conditions given by Eq. (24) and making use of $I(0) = 0$, the three constants K_0, K_1, and K_2 can be determined. These are

$$K_0 = \alpha, \qquad K_1 = \left(\tfrac{1}{2} - 8\alpha\pi^{-2}\right)I\left(\tfrac{1}{2}\pi\right) + 4\alpha\pi^{-2} - \tfrac{1}{2}$$
$$K_2 = 0 \tag{39}$$

The first-order solution is, at last,

$$F_1 = -(2\alpha/\pi)\theta + (\pi/4 - 4\alpha/\pi)\big[(\theta \cos\theta - \sin\theta)\,\ell n \tan\tfrac{1}{2}\theta$$
$$- \cos\theta I(\theta)\big] + \alpha \sin\theta + \big[\left(\tfrac{1}{2} - 8\alpha\pi^{-2}\right)I\left(\tfrac{1}{2}\pi\right)$$
$$+ 4\alpha\pi^{-2} - \tfrac{1}{2}\big]\theta \cos\theta \tag{40}$$

C. Complete Solution

The first-order corrections appearing in Eq. (40) can be added to the leading-order solution. In the interest of clarity, the resulting function and its derivatives are reproduced next. Written at $\mathcal{O}(\varepsilon^2)$, one can put

$$F(\theta) = \sin\theta + \varepsilon\{-(2\alpha/\pi)\theta + (\pi/4 - 4\alpha/\pi)$$
$$\times \big[(\theta \cos\theta - \sin\theta)\,\ell n \tan\tfrac{1}{2}\theta + \cos\theta I(\theta)\big] + \alpha \sin\theta$$
$$+ \big[\left(\tfrac{1}{2} - 8\alpha\pi^{-2}\right)I\left(\tfrac{1}{2}\pi\right) + 4\alpha\pi^{-2} - \tfrac{1}{2}\big]\theta \cos\theta\} \tag{41}$$

$$F'(\theta) = \cos\theta + \varepsilon\{2\alpha/\pi - \pi/4 + \left(\pi/4 - 4\alpha/\pi\right)\big[\sin\theta I(\theta)$$
$$- \theta \sin\theta\,\ell n \tan\tfrac{1}{2}\theta\big] + \alpha \cos\theta + \big[\left(\tfrac{1}{2} - 8\alpha\pi^{-2}\right)I\left(\tfrac{1}{2}\pi\right)$$
$$+ 4\alpha\pi^{-2} - \tfrac{1}{2}\big](\cos\theta - \theta \sin\theta)\} \tag{42}$$

$$F''(\theta) = -\sin\theta + \varepsilon\{(\pi/4 - 4\alpha/\pi)$$
$$\times \big[\cos\theta I(\theta) - (\sin\theta + \theta \cos\theta)\,\ell n \tan\tfrac{1}{2}\theta\big] - \alpha \sin\theta$$
$$- \big[\left(\tfrac{1}{2} - 8\alpha\pi^{-2}\right)I\left(\tfrac{1}{2}\pi\right) + 4\alpha\pi^{-2} - \tfrac{1}{2}\big](2\sin\theta + \theta \cos\theta)\} \tag{43}$$

$$F'''(\theta) = -\cos\theta + \varepsilon\{\left(\pi/4 - 4\alpha/\pi\right)$$
$$\times \big[-\sin\theta I(\theta) - (2\cos\theta - \theta \sin\theta)\,\ell n \tan\tfrac{1}{2}\theta - 1\big] - \alpha \cos\theta$$
$$- \big[\left(\tfrac{1}{2} - 8\alpha\pi^{-2}\right)I\left(\tfrac{1}{2}\pi\right) + 4\alpha\pi^{-2} - \tfrac{1}{2}\big](3\cos\theta - \theta \sin\theta)\} \tag{44}$$

Following Eq. (23), primes have been used to denote differentiation with respect to θ. When reverting back to y, one must use $F = F(\tfrac{1}{2}\pi y)$, $F_y = \tfrac{1}{2}\pi F'(\theta)$, $F_{yy} = \tfrac{1}{4}\pi^2 F''(\theta)$, and $F_{yyy} = \tfrac{1}{8}\pi^3 F'''(\theta)$.

The current mean-flow solution can be inserted directly into the recent oscillatory velocity and vorticity formulations obtained by Majdalani and Van Moorhem.[11] Theirs take into consideration the possible inception of oscillatory disturbances inside the porous chamber. On that account, when internal oscillations of amplitude A_p and circular frequency ω are to be accounted for the Strouhal number $Sr = \omega a/v_w$ becomes an important parameter. As shown previously,[11] the total dimensional velocity and vorticity components that include oscillatory waves can be written in the form

$$u_{tot}^* = v_w(x^*/a)F_y + [A_p/(\rho a_s)]\big[\sin(\omega x^*/a_s)\sin(\omega t)$$
$$- F \sin(\omega x^* F/a_s)\exp\chi \sin(\omega t + \Phi)\big] \tag{45}$$

$$\zeta_{tot}^* = -\left(v_w x^*/a^2\right)F_{yy}$$
$$+ [\omega A_p/(v_w \rho a_s)]\sin\left(\omega x^* F/a_s\right)\exp\chi \cos(\omega t + \Phi) \tag{46}$$

where

$$\chi(y) = \varepsilon Sr^2 \int_1^y F^{-3}(z)\,dz$$

$$\Phi(y) = Sr \int_1^y F^{-1}(z)\,dz + \varepsilon Sr\left[\frac{3}{2}(F^{-2} - 1) - 2\varepsilon Sr^2 \int_1^y F^{-5}\,dz\right]$$

$$(47)$$

For a nozzleless configuration the oscillation frequency triggered by acoustic waves is given by $\omega = (m - 1/2)\pi a_s/L$, where $m = 1, 2, \ldots$ designates the oscillation mode shape number.[6,9] For better clarity it is useful to express Eqs. (45) and (46) in terms of the familiar pressure wave amplitude $\varepsilon_p = A_p/(\rho a_s^2)$, the wall Mach number $M = v_w/a_s$, the dimensionless wave number $k = \omega a/a_s$, and normalized space coordinates. The outcome is

$$u_{tot} \equiv u_{tot}^*/v_w = xF_y + (\varepsilon_p/M)[\sin(kx)\sin(\omega t)$$
$$- F \sin(kx)\exp\chi \sin(\omega t + \Phi)] \tag{48}$$

$$\zeta_{tot} \equiv \zeta_{tot}^* v_w/a = -x F_{yy} + k\left(\varepsilon_p/M^2\right)\sin(kx F)\exp\chi \cos(\omega t + \Phi) \tag{49}$$

At this point it should be emphasized that the second term in Eq. (49) is seen to be of comparable size to the mean-flow vorticity because $\varepsilon_p M^{-2} > 1$ and $k = (m - \tfrac{1}{2})\pi a/L = \mathcal{O}(1)$. This expectation stems from the fundamental asymptotic ordering that has

been used repeatedly in aeroacoustic stability studies to linearize the Navier–Stokes equations.[1–13] This result can also be verified by recalling the classic order $M^2 < \varepsilon_p < M$ that leads to $\varepsilon_p M^{-2} > 1$. We thus realize that, while the oscillatory velocity remains small in comparison to the mean-flow contribution, the unsteady vorticity can be larger than its mean counterpart. This study also suggests that viscous dissipation constitutes an important contribution to the overall vortical field and that unsteady vorticity must not be discounted in the analysis of viscous flows in porous tubes.

V. Discussion

From the characteristic function F all flow variables can be evaluated analytically, from the foregoing formulations, and numerically, from a Runge–Kutta solver. Our numerical results use a sufficiently small tolerance to the point of making them accurate in seven significant digits. We thus consider the numerical error to be negligible.

A. Comparison at Constant Regression Ratio

Using a constant regression ratio of $\alpha = 10$, numerical and analytical solutions for F (or $-v$) and u/x (or u/u_m) are illustrated in Fig. 2. From Fig. 2a it can be inferred that Eq. (41) matches the numerical solution quite well, especially for $R > 100$. In fact, for $R \geq 500$ asymptotics and numerics become indistinguishable. Clearly, the analytical solution remains practical near an injection Reynolds number that is as low as 50. Similar trends are observed in Fig. 2b where the normalized axial velocities are compared. It appears that Eq. (42) is an adequate approximation to the exact solution. In all cases shown the largest asymptotic error occurs in the vicinity of the core and for relatively smaller values of R. These results are reassuring because they indicate an improvement in the precision of the analytical expressions at larger values of R. They become ideally suited to model the hard-blowing process in cold-flow experiments or slab rocket motors with large injection Reynolds numbers.

B. Comparison at Constant Reynolds Number

Keeping the Reynolds number fixed at several discrete values (of 100, 500, and 1000), the regression ratio is now varied from $\alpha = 0$ to a large value. Numerical and analytical solutions for u/x are depicted in Fig. 3. Figure 3a indicates that, at a low value of $R = 100$, the solution is more sensitive to the wall regression ratio than at
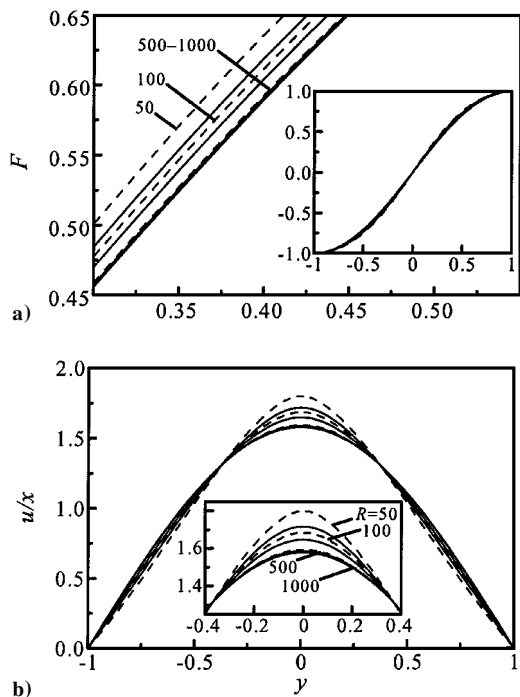
Fig. 2   Comparison between numerical (——) and analytical (- - -) solutions for a) F and b) u/x at $\alpha = 10$ and $50 \leq R \leq 1000$.
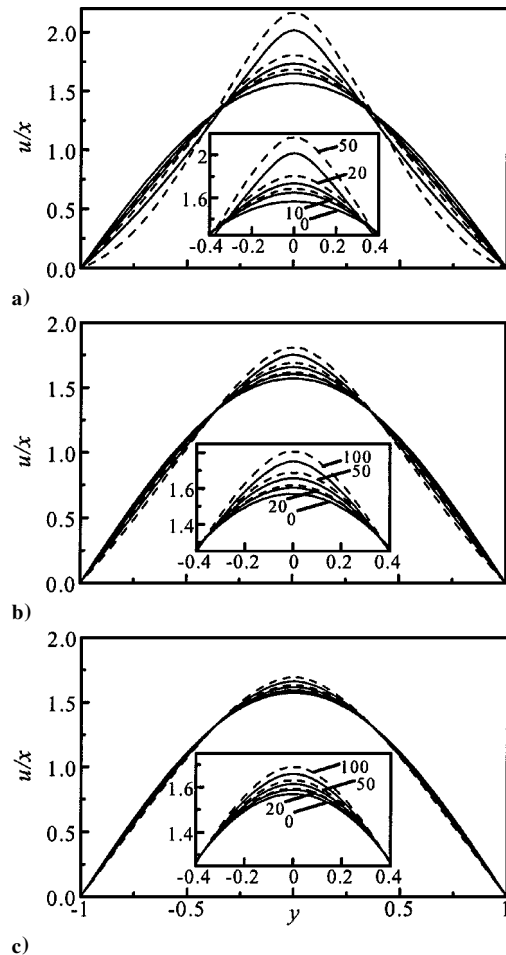
Fig. 3   Comparison between normalized axial velocities obtained from numerical (——) and analytical (- - -) solutions over a range of wall regression rates ($0 \leq \alpha \leq 100$). Here, the blowing Reynolds numbers are a) 100, b) 500, and c) 1000.

higher Reynolds numbers. In fact, for $R = 1000$ only small differences appear to exist between the $\alpha = 0$ and 100 cases. This justifies ignoring the wall regression rate in high-Reynolds-number applications. Because a value of R in excess of 1000 is not uncommon in reactive rocket motors, the assumption of a fixed boundary seems reasonable. However, for moderate R Fig. 3a indicates that noticeable differences caused by regression can occur. These differences need to be carefully accounted for by using, for instance, Eq. (42) in unison with Eq. (17).

It is clear from Fig. 3 that the accuracy of the analytical formulation deteriorates when the Reynolds number is small and the regression ratio is large. Such a physical setting is less likely to occur by virtue of $\alpha/R = 1/A \ll 1$ and the discussion presented in Sec. II. This feature can also be explained by referring the reader to the coefficient of the second term in Eq. (18). In that regard, one must recall that the relevant perturbation solution was based implicitly on the condition that $\alpha\varepsilon \ll 1$. Thus, as long as $\alpha \ll R$ one can expect the solution to be reasonably accurate. Conversely, for the impractical case of $\alpha \to R$ the analytical formulation is expected to deteriorate.

C. Flow Streamlines

To better visualize the resulting flow motion, streamlines emanating from several discrete points are shown in Figs. 4 and 5 for several values of R and α. In Fig. 4 increasing the Reynolds number at constant regression rate is seen to increase the flow turning speed. This can be explained by resorting to mass conservation. As mass is injected more rapidly into the chamber, removal of added mass near the head end requires an increasingly larger axial velocity component. Hence, to produce the necessary downstream convection the
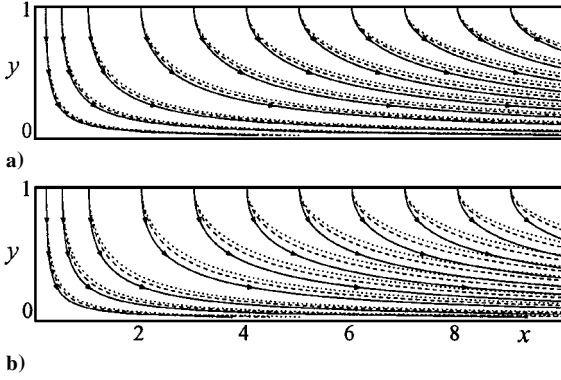
Fig. 4 Comparison between a) numerical and b) analytical streamlines for $\alpha = 10$ and $R = 20$ (——), 50 (– – –), and 1000 ($\cdots$).
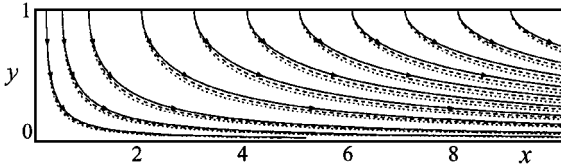

Fig. 5 Mean-flow streamlines for $R = 50$ and $\alpha = 0$ (——), 10 (- - -), and 20 ($\cdots$).

relative magnitude of the axial vs normal velocity must grow proportionately larger with successive increases in R. Because of the perturbative constraint, the agreement between Fig. 4a and Fig. 4b is excellent for $R = 1000$, but deteriorates as R is reduced to 20. An opposite effect is observed when α is varied while fixing R.

The streamline sensitivity to α is illustrated in Fig. 5. There, it can be observed that the flow turning becomes delayed when the wall regression rate is increased. This can be attributed to the fact that, when the walls expand more rapidly, the ratio of axial to normal mean-flow velocities is reduced. In theory, the diminution in axial velocity can continue until this ratio has vanished. That hypothetical case takes place when the relative fluid velocity at the wall is exactly offset by the speed of the expanding walls.

VI. Additional Flow Properties

Having characterized the velocity field, the remaining flow properties, such as pressure and stress distributions, can now be examined.

A. Normal Pressure Distribution

The normal pressure gradient can be obtained by substituting the velocity components into Eq. (3). Because of the dependence of the normalized variables on time, one must proceed carefully with the chain derivatives. These include

$$\frac{a}{v_w}\frac{\partial v}{\partial t} = -\frac{a}{v_w}F_t = \varepsilon\alpha(F + yF_y), \qquad \frac{\partial v}{\partial x} = 0$$

$$\frac{\partial^2 v}{\partial x^2} = 0, \qquad v\frac{\partial v}{\partial y} = FF_y, \qquad \frac{\partial^2 v}{\partial y^2} = -F_{yy} \quad (50)$$

Following substitution into Eq. (3), a simple rearrangement yields

$$p_y = -[\varepsilon F_{yy} + FF_y + \alpha\varepsilon(F + yF_y)] \quad (51)$$

The normal pressure distribution can now be determined by integrating Eq. (51) while observing the boundary conditions given by Eq. (19). Letting p_c be the centerline pressure, one can proceed from

$$\int_{p_c}^{p} dp = \int_{0}^{y} -[\varepsilon F_{yy} + FF_y + \alpha\varepsilon(F + yF_y)]\,dy \quad (52)$$
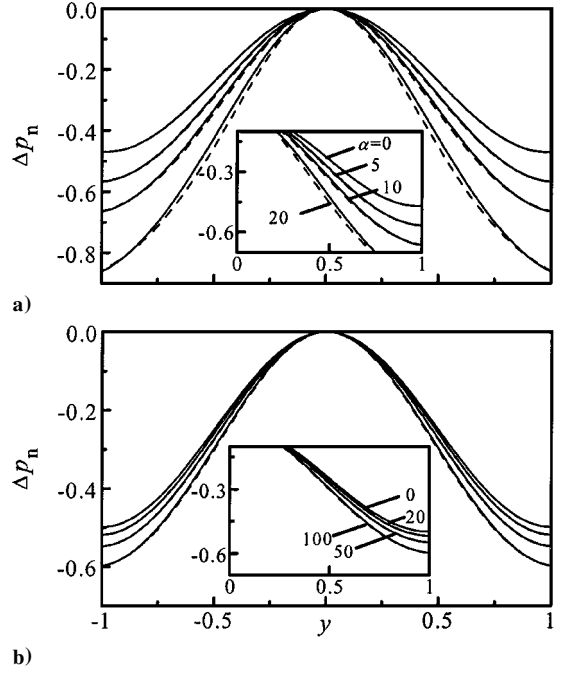

Fig. 6 Comparison between numerical (——) and analytical (- - -) pressure drops in the normal direction for a) $R = 50$ and b) $R = 1000$. Enlargements are shown in the inset.

Using $FF_y = \frac{1}{2}(F^2)_y$ and $(F + yF_y) = (yF)_y$, one can integrate Eq. (52) directly into

$$\Delta p_n = \varepsilon F_y(0) - \left(\varepsilon F_y + \tfrac{1}{2}F^2 + \alpha\varepsilon yF\right) \quad (53)$$

Figure 6 illustrates the pressure distribution for several levels of injection and regression. For every level of injection, the absolute pressure drop is largest near the walls. Increasing the regression ratio also increases the pressure drop. Comparing Fig. 6a to Fig. 6b, the sensitivity of the pressure to variations in wall expansion appears to be less significant at high Reynolds numbers. Because of the uniform agreement between numerics and asymptotics, the two types can be hardly discerned except for small R and large α (Fig. 6a). Also, for small $\varepsilon\alpha$ the normal pressure gradient is near zero at the wall.

B. Axial Pressure Distribution

Similar substitutions into Eq. (2) give rise to a closed-form expression for the axial pressure gradient. Using

$$\frac{\partial y}{\partial t} = -\frac{\dot{a}y}{a}$$

$$\frac{a}{v_w}u_t = \frac{a}{v_w}(xF_y)_t = -x\varepsilon\alpha(yF_{yy} + 2F_y) \quad (54)$$

the pressure gradient can be derived from the axial momentum equation

$$p_x = x\left[\varepsilon F_{yyy} + FF_{yy} - (F_y)^2 + \alpha\varepsilon(2F_y + yF_{yy})\right] \quad (55)$$

Equation (55) can, in turn, be integrated to obtain an axial pressure distribution at any spatial location:

$$\Delta p_a = \tfrac{1}{2}x^2\left[\varepsilon F_{yyy} + FF_{yy} - (F_y)^2 + \alpha\varepsilon(2F_y + yF_{yy})\right] \quad (56)$$

The character of the axial pressure distribution is similar to that of Eq. (53).

C. Shear Stress and Vorticity Distributions

Starting with Newton's equation for shear stress, one can substitute the velocity and write $\tau = \tau^*/(\rho v_w^2) = \varepsilon xF_{yy} = -\varepsilon\zeta$, where
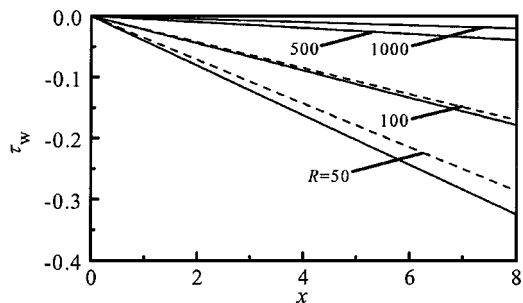
Fig. 7 Comparison between numerical (——) and analytical (- - -) wall shear stresses for $\alpha = 10$ and a range of R.

Eq. (17) has been used for the mean-flow vorticity. The proportionality constant that exists between shear and vorticity is $-\varepsilon$. At the wall the stress becomes $\tau_w = \varepsilon x F_{yy}(1) = -\varepsilon \zeta(1)$.

A plot of the wall shear stress is shown in Fig. 7 for a fixed value of α and a range of R. As the Reynolds number becomes very large, the role of viscosity diminishes, and the shear (or vorticity) at the wall becomes less appreciable. The agreement between asymptotics and numerics also improves with increasing R.

VII.   Conclusions

In this paper an exact similarity solution to the Navier–Stokes equations is presented. The problem arises in the context of an injection-driven flow inside a porous chamber with regressing walls. The similarity transformations in space and time turn the momentum equations into a single, nonlinear, differential equation. The resulting equation reduces to the classic Berman formula for a channel with stationary walls. Closed-form expressions obtained using regular perturbations and the method of variation of parameters are shown to coincide with the numerical solution over a useful range of parameters. Because of their adequate accuracy, these explicit formulations are practically equivalent to the exact solution, especially when the ratio of regression and injection parameters (α/R) is small. Clearly, when injection is increased the effect of varying the regression rate becomes less pronounced. Larger values of R also improve the accuracy of the analytical expressions. Their improved precision makes them suitable for modeling the hard-blowing process and hydrodynamic instability in slab rocket motors and cold-flow experiments. When inserted into the oscillatory vortico-acoustic wave solution for rocket chambers, a consistently rotational and viscous field is realized in both mean and time-dependent components. This leads to a more precise assessment of the unsteady vorticity field that is strongly influenced by the amount of viscous dissipation. Our study also suggests that both unsteady and inviscid-flow vorticity components must be retained in a full-scale analysis because of their comparable orders. It is hoped that the complete solution can be later used, instead of the inviscid profile, to investigate hydrodynamic instability and transition to turbulence. In what regards streamline behavior, it is found that increasing the Reynolds number accelerates flow turning and leads to a larger flow energy consumption. Conversely, increasing wall regression promotes a delayed response that can be associated with a smaller flow turning loss. Because the traditional flow turning mechanism is considered a sink of acoustic energy, this study suggests that faster burning propellants are prone to a larger destabilizing energy. Regarding the sensitivity of the viscous solution to regression rates up to 100, it is found that, for Reynolds numbers in excess of 1000, the mean-flow velocity becomes practically equivalent to Taylor's inviscid profile irrespective of the regression rate. This justifies the traditional use of Taylor's solution in certain applications. However, for $R < 1000$ discrepancies with the inviscid profile begin to appear. These deviations become appreciable for $R < 500$ and intolerable for $R < 100$. Under such conditions the viscous mean-flow solution ought to be substituted. Aside from the technical merit in modeling chamber gas dynamics, the solutions precipitated from this study are hoped to increase our repertory of known approximations for laminar flows in porous channels and tubes.

References

[1]Flandro, G. A., "Effects of Vorticity on Rocket Combustion Stability," *Journal of Propulsion and Power*, Vol. 11, No. 4, 1995, pp. 607–625.

[2]Flandro, G. A., "On Flow Turning," AIAA Paper 95-2530, July 1995.

[3]Flandro, G. A., "Effects of Vorticity Transport on Axial Acoustic Waves in a Solid Propellant Rocket Chamber," *Combustion Instabilities Driven by Thermo-Chemical Acoustic Sources*, NCA, Vol. 4, HTD Vol. 128, American Society of Mechanical Engineers, New York, 1989, pp. 53–61.

[4]Majdalani, J., "The Boundary Layer Structure in Cylindrical Rocket Motors," *AIAA Journal*, Vol. 37, No. 4, 1999, pp. 505–508.

[5]Majdalani, J., "Vortical and Acoustical Mode Coupling Inside a Two-Dimensional Cavity with Transpiring Walls," *Journal of the Acoustical Society of America*, Vol. 106, No. 1, 1999, pp. 46–56.

[6]Majdalani, J., "Vorticity Dynamics in Isobarically Closed Porous Channels. Pt 1: Standard Perturbations," *Journal of Propulsion and Power*, Vol. 17, No. 2, 2001, pp. 355–362.

[7]Majdalani, J., "Asymptotic Formulation for an Acoustically Driven Field Inside a Rectangular Cavity with a Well-Defined Convective Mean Flow Motion," *Journal of Sound and Vibration*, Vol. 223, No. 1, 1999, pp. 73–95.

[8]Majdalani, J., "The Oscillatory Channel Flow with Arbitrary Wall Injection," *Journal of Applied Mathematics and Physics*, Vol. 52, No. 1, 2001, pp. 33–61.

[9]Majdalani, J., and Roh, T. S., "Vorticity Dynamics in Isobarically Closed Porous Channels. Pt 2: Space-Reductive Perturbations," *Journal of Propulsion and Power*, Vol. 17, No. 2, 2001, pp. 363–370.

[10]Majdalani, J., and Roh, T. S., "The Oscillatory Channel Flow with Large Wall Injection," *Proceedings of the Royal Society, Series A*, Vol. 456, No. 1999, 2000, pp. 1625–1657.

[11]Majdalani, J., and Van Moorhem, W. K., "Laminar Cold-Flow Model for the Internal Gas Dynamics of a Slab Rocket Motor," *Journal of Aerospace Science and Technology*, Vol. 5, No. 3, 2001, pp. 193–207.

[12]Majdalani, J., and Van Moorhem, W. K., "Improved Time-Dependent Flowfield Solution for Solid Rocket Motors," *AIAA Journal*, Vol. 36, No. 2, 1998, pp. 241–248.

[13]Majdalani, J., and Van Moorhem, W. K., "A Multiple-Scales Solution to the Acoustic Boundary Layer in Solid Rocket Motors," *Journal of Propulsion and Power*, Vol. 13, No. 2, 1997, pp. 186–193.

[14]Apte, S., and Yang, V., "Effect of Acoustic Oscillation on Flow Development in a Simulated Nozzleless Rocket Motor," *Solid Propellant Chemistry, Combustion, and Motor Interior Ballistics*, edited by V. Yang, T. B. Brill, and W.-Z. Ren, Progress in Astronautics and Aeronautics, Vol. 185, AIAA, Reston, VA, 2000, pp. 791–822.

[15]Apte, S., and Yang, V., "Unsteady Flow Evolution in Porous Chamber with Surface Mass Injection. Pt 1: Free Oscillation," *AIAA Journal*, Vol. 39, No. 8, 2001, pp. 1577–1586.

[16]Apte, S., and Yang, V., "Unsteady Flow Evolution in Porous Chamber with Surface Mass Injection. Pt 2: Acoustic Excitation," *AIAA Journal*, Vol. 40, No. 2, 2002, pp. 244–253.

[17]Beddini, R. A., "Injection-Induced Flows in Porous-Walled Ducts," *AIAA Journal*, Vol. 24, No. 11, 1986, pp. 1766–1773.

[18]Sabnis, J. S., and Eagar, M. A., "Evolution of Internal Flow in a Solid Rocket Motor with Radial Slots," *Journal of Propulsion and Power*, Vol. 12, No. 4, 1996, pp. 632–637.

[19]Avalon, G., Casalis, G., and Griffond, J., "Flow Instabilities and Acoustic Resonance of Channels with Wall Injection," AIAA Paper 98-3218, July 1998.

[20]Casalis, G., Avalon, G., and Pineau, J.-P., "Spatial Instability of Planar Channel Flow with Fluid Injection through Porous Walls," *Physics of Fluids*, Vol. 10, No. 10, 1998, pp. 2558–2568.

[21]Griffond, J., and Casalis, G., "On the Dependence on the Formulation of Some Nonparallel Stability Approaches Applied to the Taylor Flow," *Physics of Fluids*, Vol. 12, No. 2, 2000, pp. 466–468.

[22]Griffond, J., and Casalis, G., "On the Nonparallel Stability of the Injection Induced Two-Dimensional Taylor Flow," *Physics of Fluids*, Vol. 13, No. 6, 2001, pp. 1635–1644.

[23]Liou, T.-M., and Lien, W.-Y., "Numerical Simulations of Injection-Driven Flows in a Two-Dimensional Nozzleless Solid-Rocket Motor," *Journal of Propulsion and Power*, Vol. 11, No. 4, 1995, pp. 600–606.

[24]Liou, T. M., Lien, W. Y., and Hwang, P. W., "Large-Eddy Simulations of Turbulent Reacting Flows in a Chamber with Gaseous Ethylene Injecting Through the Porous Wall," *Combustion and Flame*, Vol. 99, No. 3–4, 1994, pp. 591–600.

[25]Liou, T. M., Lien, W. Y., and Hwang, P. W., "Transition Characteristics of Flowfield in a Simulated Solid-Rocket Motor," *Journal of Propulsion and Power*, Vol. 14, No. 3, 1998, pp. 282–289.

[26]Buckmaster, J., Jackson, T. L., and Ulrich, M., "Numerical Modeling of Heterogeneous Propellant Combustion," AIAA Paper 2001-3579, July 2001.

[27]Jackson, T. L., Buckmaster, J., Campbell, M., Kochevets, S., and Massa, L., "The Burning of 3d Random-Pack Heterogeneous Propellants," AIAA Paper 2001-3952, July 2001.

[28]Beckstead, M., "Overview of Combustion Mechanisms and Flame Structures for Advanced Solid Propellants," *Solid Propellant Chemistry, Combustion, and Motor Interior Ballistics*, edited by V. Yang, T. B. Brill, and W.-Z. Ren, Progress in Astronautics and Aeronautics, Vol. 185, Reston, VA, 2000, pp. 267–285.

[29]Yuan, S. W., "Further Investigation of Laminar Flow in Channels with Porous Walls," *Journal of Applied Physics*, Vol. 27, No. 3, 1956, pp. 267–269.

[30]Berman, A. S., "Laminar Flow in Channels with Porous Walls," *Journal of Applied Physics*, Vol. 24, No. 9, 1953, pp. 1232–1235.

[31]Yuan, S. W., and Finkelstein, A. B., "Laminar Pipe Flow with Injection and Suction Through a Porous Wall," *Transactions of the American Society of Mechanical Engineers: Journal of Applied Mechanics, Series E*, Vol. 78, No. 3, 1956, pp. 719–724.

[32]Goto, M., and Uchida, S., "Unsteady Flows in a Semi-Infinite Expanding Pipe with Injection through Wall," *Transactions of the Japan Society for Aeronautical and Space Sciences*, Vol. 33, No. 9, 1990, pp. 14–27.

[33]Taylor, G. I., "Fluid Flow in Regions Bounded by Porous Surfaces," *Proceedings of the Royal Society, London, Series A*, Vol. 234, No. 1199, 1956, pp. 456–475.

[34]Uchida, S., and Aoki, H., "Unsteady Flows in a Semi-Infinite Contract-ing or Expanding Pipe," *Journal of Fluid Mechanics*, Vol. 82, No. 2, 1977, pp. 371–387.

[35]Barron, J., Majdalani, J., and Van Moorhem, W. K., "A Novel Investi-gation of the Oscillatory Field over a Transpiring Surface," *Journal of Sound and Vibration*, Vol. 235, No. 2, 2000, pp. 281–297.

[36]Majdalani, J., Barron, J., and Van Moorhem, W. K., "Experimental Classification of Turbulence in an Oscillatory Channel Flow with Transpiring Walls," American Society of Mechanical Engineers FEDSM Paper 2001-1881, May–June 2001.

[37]Ma, Y., Van Moorhem, W. K., and Shorthill, R. W., "Innovative Method of Investigating the Role of Turbulence in the Velocity Coupling Phe-nomenon," *Journal of Vibration and Acoustics*, Vol. 112, No. 4, 1990, pp. 550–555.

[38]Ma, Y., Van Moorhem, W. K., and Shorthill, R. W., "Experimental Investigation of Velocity Coupling in Combustion Instability," *Journal of Propulsion and Power*, Vol. 7, No. 5, 1991, pp. 692–699.

[39]Sutton, G. P., *Rocket Propulsion Elements*, 6th ed., Wiley, New York, 1992, p. 418.

[40]Reid, R. C., Prausnitz, J. M., and Poling, B. E., *The Properties of Gases and Liquids*, 4th ed., McGraw–Hill, New York, 1987, pp. 388–490.

[41]Goto, M., and Uchida, S., "Unsteady Flow in a Semi-Infinite Contract-ing or Expanding Pipe with a Porous Wall," *Proceedings of the 40th Japan National Congress for Applied Mechanics*, Vol. NCTAM-40, Japan National Congress for Applied Mechanics, Tokyo, Japan, 1990, pp. 163–172.